



# Thermal equation of state of phase egg (AlSiO<sub>3</sub>OH): implications for hydrous phases in the deep earth

Yungui Liu<sup>1,2</sup> · Rong Huang<sup>3</sup> · Ye Wu<sup>4</sup> · Dongzhou Zhang<sup>5</sup> · Junfeng Zhang<sup>1</sup> · Xiang Wu<sup>1</sup>

Received: 26 April 2020 / Accepted: 12 November 2020 / Published online: 10 January 2021  
© Springer-Verlag GmbH Germany, part of Springer Nature 2021

## Abstract

Phase egg (AlSiO<sub>3</sub>OH), an important hydrous phase in the Al<sub>2</sub>O<sub>3</sub>–SiO<sub>2</sub>–H<sub>2</sub>O ternary system, was found in the superdeep diamond from the mantle transition zone. Here, we have investigated the compressibility and the crystal structural evolution of phase egg using the synchrotron-based single-crystal X-ray diffraction and infrared spectroscopy combined with diamond anvil cells up to 32 GPa and 900 K. Present results show that the hydrogen atom flips its position and forms a new hydrogen bond configuration at ~14 GPa and room temperature, leading to a first-order phase transition of phase egg, but this behavior is smeared out because of thermal disordering of hydrogen atom at high temperatures. These findings provide important implications for revealing the complex state of hydrogen in the deep earth. Along the cold and warm subducting slab geotherms, the density and bulk velocity of phase egg are greater than those of preliminary reference Earth model in the mantle transition zone, presenting negative buoyancy force for deep-water transportation. Based on the obtained thermal elastic parameters, we further demonstrate that topaz-OH transforms to phase egg with a ~11.7% increase in bulk velocity and a ~4.2% increase in density, and phase egg decomposes into δ-AlOOH and stishovite with a ~6.2% increase in bulk velocity and a ~4.0% increase in density under subduction zone conditions.

**Keywords** Phase egg · Mantle transition zone · Hydrogen bond · Subducting slab

---

Communicated by Gordon Moore.

**Supplementary Information** The online version contains supplementary material available at <https://doi.org/10.1007/s00410-020-01758-1>.

✉ Xiang Wu  
wuxiang@cug.edu.cn

- <sup>1</sup> State Key Laboratory of Geological Processes and Mineral Resources, China University of Geosciences (Wuhan), Wuhan 430074, China
- <sup>2</sup> College of Gems and Materials, Hebei GEO University, Shijiazhuang 050031, China
- <sup>3</sup> Bayerisches Geoinstitut, University of Bayreuth, 95447 Bayreuth, Germany
- <sup>4</sup> School of Science, Wuhan University of Technology, Wuhan 430074, China
- <sup>5</sup> School of Ocean and Earth Science and Technology, Hawai'i Institute of Geophysics and Planetology, University of Hawai'i at Manoa, Honolulu, HI 96822, USA

## Introduction

The occurrence and distribution of water in Earth's interior is one of the most important topics in mineral physics, geophysics and geodynamics, because it significantly affects the elasticity, rheology and transport properties of minerals at high-pressure and high-temperature (HPHT) conditions (e.g., Ohtani 2005; Litasov and Ohtani 2007; Liu et al. 2018; Muir and Brodholt 2018). Recently, observations of hydrous ringwoodite and ice-VII inclusions in the superdeep diamonds have provided direct evidences to support a hydrous mantle transition zone, at least locally beneath subduction zones (Pearson et al. 2014; Tschauner et al. 2018). One source of the water (or hydrogen) in the deep earth is believed to be the Earth's surface (e.g., sediments and oceanic crusts) and such surface water is transported to the deep earth by subducting slabs (Ohtani et al. 2004; Faccenda 2014; Howe and Pawley 2019). Though sediments dehydrate significantly at depths shallower than 230 km (van Keken et al. 2011; Yoshino et al. 2019), according to the HPHT experiments, aluminous hydrous phases in pelagic sediments of the Al<sub>2</sub>O<sub>3</sub>–SiO<sub>2</sub>–H<sub>2</sub>O (ASH) system are known

to be stable in the deep earth (Ohtani et al. 2001; Pamato et al. 2014; Fukuyama et al. 2017) and even at the bottom of the lower mantle (Duan et al. 2018), or the rehydration of subducted sediments may occur and help to reserve water (Yoshino et al. 2019). HPHT experiments on hydrated sedimentary rocks suggested that topaz-OH ( $\text{Al}_2\text{SiO}_4(\text{OH})_2$ ) is likely to be stable up to 12 GPa and then transforms to the high-pressure hydrous aluminosilicate mineral phase egg (ideal formula is  $\text{AlSiO}_3\text{OH}$ ) (Ono 1998). Phase egg is stable up to 23 GPa above 1473 K, and then decomposes into stishovite and  $\delta$ - $\text{AlOOH}$  (Sano et al. 2004). Further experiments demonstrate that  $\delta$ - $\text{AlOOH}$  is stable at the whole lower mantle  $P$ - $T$  conditions and decomposes at the core-mantle boundary (Nishi et al. 2014; Duan et al. 2018). Phase egg, as a classic aluminous hydrous phase in ASH ternary system, plays a key role in water transportation at the depth of mantle transition zone. Thus, the properties of phase egg, such as structural stability and sound velocity, can provide important constraints on deep water cycle and seismic velocity anomalies in the mantle transition zone (Fukuyama et al. 2017; Mookherjee et al. 2019).

Phase egg (space group  $P2_1/n$  and  $Z=4$ ) was first synthesized by Eggleton et al. (1978) at approximately 1273 K and pressures greater than 10 GPa. It is hence named after Eggleton (Schmidt et al. 1995). In 2007, tetragonal phase egg as nanocrystalline inclusion was found in the superdeep diamond from Rio Soriso, Juina area, Brazil (Wirth et al. 2007). The ideal phase egg  $\text{AlSiO}_3\text{OH}$  contains 7.5 wt%  $\text{H}_2\text{O}$  and hydrogen atoms lie in the vacant spaces formed by the corner linked columns consisting of edge-shared octahedra (Schmidt et al. 1998). Previous studies show that phase egg is stable at relevant  $P$ - $T$  conditions of the mantle transition zone (Sano et al. 2004; Fukuyama et al. 2017) or even down to the top of the lower mantle (Pamato et al. 2014). The compressibility of phase egg at room temperature has been studied based on the powder X-ray diffraction (XRD) up to 40 GPa (Vanpeteghem et al. 2003) and single-crystal XRD with a maximum pressure of 23 GPa (Schulze et al. 2018). Both experimental results have confirmed the anisotropic compression response of phase egg, i.e., the shortest unit-cell axis  $b$  is the most compressible direction and the longest unit-cell axis  $a$  is the hardest direction. Previous studies are consistent in bulk modulus  $K_0$  using the third-order Birch–Murnaghan equation of state (B–M EoS), but have a relatively large discrepancy in the pressure derivative of bulk modulus  $K'$  (6.5 from powder XRD, Vanpeteghem et al. 2003; 8.6 from single-crystal XRD, Schulze et al. 2018). A recent first-principle simulation based on density functional theory indicates that phase egg exhibits an anomalous behavior in the pressure dependence of the elasticity at approximately 15 GPa, which is attributed to the change of hydrogen bond configuration (Mookherjee et al. 2019). It is necessary to carry out experimental simulations to constrain

the relationship between the hydrogen bond behavior and the compressibility, especially at relevant mantle temperatures. Study on the structure and elasticity of phase egg under HPHT conditions is also essential to understand its influences on subduction zones.

Here we present single-crystal XRD and infrared spectroscopy (IR) experiments of phase egg up to 25 GPa at room temperature to reveal its detailed structure and crystal chemistry properties. We have also measured its thermal equation of state up to approximately 32 GPa and 900 K using an externally heated diamond anvil cell (DAC). From the data we obtain the thermal elastic parameters, hydrogen bond evolution, axial compressibility, density, and bulk velocity of phase egg at mantle conditions. Based on these results, we discuss the state of hydrogen in phase egg at the conditions of Earth's interior and its geophysical implications.

## Materials and methods

### Samples synthesis and characterizations

High-quality single-crystal phase egg samples labeled S6946 were synthesized using a kawai-type multi-anvil press at the Bayerisches Geoinstitut (BGI), University of Bayreuth, Germany. We mixed the powder of  $\text{Al}(\text{OH})_3\text{:SiO}_2$  in a molar ratio of 1:1, and then loaded it into an  $\text{Au}_{80}\text{Pd}_{20}$  capsule that is 2 mm in length and 1.6 mm in diameter. A Cr-doped MgO octahedron with an edge length of 10 mm was adopted as pressure medium. Eight tungsten carbide anvils with a truncation of 5 mm were used as the second-stage anvils and  $\text{LaCrO}_3$  was used as the heater. This assembly was compressed to 19 GPa and then heated to 1373 K for 6 h. The recovered samples were colorless single crystals with small grain sizes of 10–80  $\mu\text{m}$ . Sample characterizations were performed at ambient conditions using scanning electron microscope (SEM) equipped with energy dispersive spectrometer (EDS) (Quanta 450 FEG), XRD (Rigaku XtaLAB PRO MM007HF) and Raman spectroscopy (Horiba LabRAM HR Evolution). The SEM and EDS results indicated that samples were chemically homogeneous with polyhedral shape (Fig. S1) and the average ratio of Al to Si of 10 grains is 0.99:1, the chemical formula of phase egg is normalized to  $\text{Al}_{0.99}\text{SiO}_4\text{H}_{1.03}$  accordingly. The crystal structure was determined to be monoclinic phase ( $P2_1/n$  and  $Z=4$ ) with lattice constants of  $a=7.1500(6)$   $\text{\AA}$ ,  $b=4.3309(3)$   $\text{\AA}$ ,  $c=6.9517(6)$   $\text{\AA}$ ,  $\beta=98.348(8)^\circ$  and  $V=212.99(3)$   $\text{\AA}^3$  by a micro-focused X-ray diffractometer equipped with Mo  $K\alpha$  radiation. The unit-cell volume in this study is slightly smaller than that of  $\text{Al}_{0.98}\text{Si}_{0.92}\text{O}_3\text{OH}_{1.39}$  (214.43  $\text{\AA}^3$ ) reported by Schulze et al. (2018), but agrees well with that of  $\text{Al}_{0.99}\text{Si}_{1.01}\text{O}_3\text{OH}_{0.99}$  (212.99  $\text{\AA}^3$ ) (Schmidt et al. 1998). Raman spectra of 12

grains picked randomly were the same and in agreement with the results reported by Xue et al. (2006) (Fig. S2).

### High-pressure synchrotron radiation XRD experiments

A short symmetry-type DAC fitted with Boehler-type diamond anvils of 400- $\mu\text{m}$  flat culets with 60° opening was employed to achieve high pressure at room temperature experiments. A hole of 240- $\mu\text{m}$ -diameter was drilled in the pre-indented rhenium gasket of 39  $\mu\text{m}$  thickness as the sample chamber. A single-crystal sample of grain size  $\sim 20 \times 20 \times 15 \mu\text{m}^3$  was loaded into the sample chamber, as well as a piece of platinum for pressure calibration (Fei et al. 2007). Neon was employed as the pressure transmitting medium using the COMPRES/GSECARS gas-loading system and ruby sphere was used as the pressure indicator (Rivers et al. 2008; Mao et al. 1986). In situ high-pressure single-crystal XRD experiments were carried out at beamline 16-IDB at Advanced Photon Source (APS), Argonne National Laboratory (ANL). A monochromatic X-ray beam with the wavelength of 0.40663 Å was focused on a  $5.5 \times 3.2 \mu\text{m}^2$  spot. XRD patterns were recorded with the Pilatus detector on compression and the MAR165 charge-coupled device detector on decompression. Wide-scan and stepped exposures were collected in a rotation range from  $-30^\circ$  to  $30^\circ$  in  $1^\circ$  steps, and the exposure time was one second per degree. Experimental data were analyzed using the GSE\_ADA/RSV software package (Dera et al. 2013). Polarization, Lorentz and empirically determined diamond absorption corrections were applied to the peak intensities. Lattice parameters and the orientation matrix were obtained using RSV. Crystal structure refinements were performed on the decompression data by SHELXL software facilitated by Olex2 general user interface at five different pressures (Dolomanov et al. 2009). The resulting discrepancy factors,  $R_1$ , varied between 3.27 and 7.35% with  $R_{\text{int}}$  ranged from 3.11 to 5.08%. The crystal chemical characters of bond lengths and distortions were calculated by the VESTA software (Momma and Izumi 2008). The wide-scan diffraction patterns were indexed using the GSE\_ADA program and the lattice parameters were calculated by the program Unit Cell (Holland and Redfern 1997).

### HPHT synchrotron radiation XRD experiments

In situ HPHT single-crystal XRD experiments were conducted up to 32 GPa at five given temperatures of 300 K, 450 K, 600 K, 750 K and 900 K at beamline 13-BMC at APS, ANL. A BX90-type DAC also fitted with 400- $\mu\text{m}$  flat culets diamond anvils was used combined with external heater. A single-crystal sample polished on both sides of grain size  $\sim 30 \times 30 \times 15 \mu\text{m}^3$  was loaded into the chamber which was prepared in the

same steps as the room-temperature experiments. Platinum and neon were employed as the pressure calibration and pressure transmitting medium, respectively. Alumina ceramic coiled by one platinum wire of 200  $\mu\text{m}$  in diameter and  $\sim 45 \text{ cm}$  in length was used as the heater where the resistance was approximately  $2 \Omega$ . K-type thermocouple attached to one of the diamond anvils was used to determine the temperatures. The GE membrane pressure controller for DAC at beamline 13-BMC was employed to automatically increase the pressure. We increased the temperature to three (or four) expected value at a given original pressure and cooled to 300 K after this run, then we increased the pressure to a higher value for a new run. For each heating run, the sample chamber was stabilized for at least 20 min at the given temperature to minimize temperature gradient and pressure instability. A monochromatic X-ray beam with the wavelength of 0.43409 Å was focused on an approximately  $15 \times 15 \mu\text{m}^2$  spot and XRD patterns were recorded with the Pilatus3 1 M detector. Due to the limitation of heater geometry and diamond anvil cell opening angle, 3D-reconstruction of the lattice in reciprocal space and reliable structural refinement are unavailable with the GSE\_ADA/RSV software package. The collected patterns were integrated using the program FIT 2D (Hammersley 2016) and then Unit Cell program (Holland and Redfern 1997) was used to calculate the lattice parameters.

### High-pressure synchrotron radiation IR experiments

A BX90-type DAC fitted with 300- $\mu\text{m}$  flat culets Moissanite (SiC) anvils was used for high pressure IR experiments which were carried out at beamline BL01B at national synchrotron radiation laboratory (NSRL), China. A hole of 150- $\mu\text{m}$ -diameter was drilled in the pre-indented rhenium gasket of 38  $\mu\text{m}$  thickness as the sample chamber and a single-crystal sample of grain size  $\sim 20 \times 40 \times 20 \mu\text{m}^3$  was loaded. Argon was employed as the pressure transmitting medium and ruby sphere was used as the pressure indicator (Mao et al. 1986). IR spectra in the frequency range 5500–700  $\text{cm}^{-1}$  were obtained using a Bruker 66 V spectrometer coupled with a KBr beam-splitter and liquid-nitrogen cooled FPA detector. The aperture size was set to be  $20 \times 20 \mu\text{m}^2$ . In each measurement, 256 scans were acquired with 4  $\text{cm}^{-1}$  resolution, and the background spectra were measured through the SiC inside the Argon-filled gasket hole.

## Results and discussion

### Equation of state

Phase egg was compressed up to 25 GPa at room temperature. The unit-cell volumes of phase egg monotonously

decrease with increasing pressure (Fig. 1 and Table S1), which is fitted to the B-M EoS to get the elastic parameters (Angel et al. 2014). The fitting results are as follows with  $V_0$  fixed at  $212.99 \text{ \AA}^3$ :  $K_0 = 160(3) \text{ GPa}$  and  $K' = 8.8(4)$  for the third-order B-M EoS and  $K_0 = 190(2) \text{ GPa}$  for the second-order B-M EoS with a fixed  $K' = 4$ . The derived third-order B-M EoS parameters are in good agreement with the previous values from single-crystal XRD data (Schulze et al. 2018), while the first pressure derivative  $K'$  is larger than the powder XRD results (Vanpeteghem et al. 2003). However, compared to the  $P$ - $V$  fitting curve of third-order and second-order B-M EoS, a kink on the  $P$ - $V$  data was observed at approximately 14 GPa. Therefore, we fitted the data below 14 GPa to a third-order B-M EoS and yielded:  $K_0 = 169(2) \text{ GPa}$  and  $K' = 6.6(6)$ . The difference of the first pressure derivative  $K'$  between the fitting results below 14 GPa and all data confirm the change in compressibility of phase egg (Hushur et al. 2011). This critical pressure is also consistent with that of a first-order phase transition caused by the proton flipping (Mookherjee et al. 2019). Such transition is often associated with discontinuity in second-order derivatives of bulk modulus. To further confirm this transition, the second-order B-M EoS has been used to fit our data below and above 14 GPa, respectively. The fitting yields:  $V_0 = 212.94(6) \text{ \AA}^3$  and  $K_0 = 181(2) \text{ GPa}$  for the data below 14 GPa and  $V_0 = 209.8(4) \text{ \AA}^3$  and  $K_0 = 244(7) \text{ GPa}$  for those from 14 to 25 GPa. In a word, our fitting results are

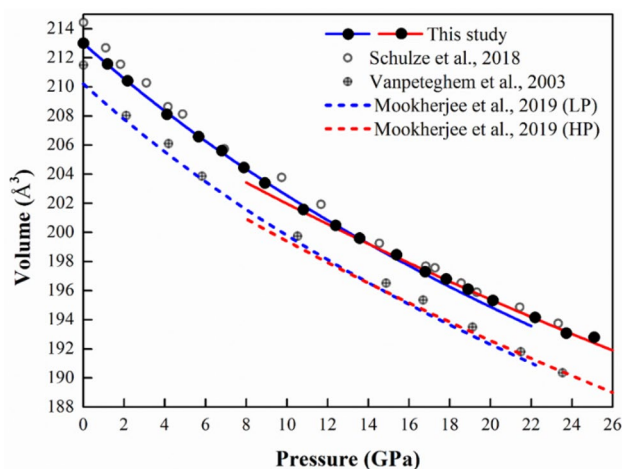


**Fig. 1** Unit-cell volumes of phase egg as a function of pressure. The solid black and open gray circles and the circles with cross represent the experimental data from this study, Schulze et al. (2018) and Vanpeteghem et al. (2003), respectively. The solid blue and red line represent the fitting results from our data using third-order B-M EoS for 0–14 GPa and second-order B-M EoS for 14–25 GPa, respectively. The dashed blue and red line represent the results from literature data (Mookherjee et al. 2019) using third-order B-M EoS for 0–15 GPa (LP) and 15–25 GPa (HP). Error bars are smaller than the symbol size for our data

consistent well with those of theoretical calculation results at 0 K (Fig. 1) (Mookherjee et al. 2019).

Figure 2 plots unit-cell volumes of phase egg at HPHT conditions (data presented in Table S2). We fitted the experimental data using third-order B-M thermal equation of state (Text S1) up to 35 GPa and 900 K (Angel et al. 2014). The thermoelastic parameters derived from the fitting with  $V_0$  fixed at  $212.99 \text{ \AA}^3$  are as follows:  $K_0 = 167(8) \text{ GPa}$ ,  $K' = 5.5(10)$ ,  $\partial K/\partial T = -0.023(5) \text{ GPa/K}$ ,  $\alpha_0 = 4.2(11) \times 10^{-5} \text{ K}^{-1}$ . The bulk modulus and first pressure derivative derived from the thermal equation of state are consistent with the fitting results based on the experimental data from 0 to 14 GPa at room temperature within accepted uncertainties. We note that the kink found at  $\sim 14 \text{ GPa}$  in the  $P$ - $V$  data at room temperature is not observed in all of the  $P$ - $V$  data from HPHT experiments. The hydrogen atom might be in a state of thermally induced disordering under high temperature condition, which might smear over the hydrogen bond configuration. This disordered behavior can be attributed to the exquisite sensitivity of hydrogen bond to both temperature and pressure (Dougherty 1998). Thus, it is more likely that the transition still occurs same as the behavior at room temperature, or the transfer of proton is suppressed by high temperature, we lack sufficient evidence to determine whether the proton flips its position at HPHT conditions. But the complex state of hydrogen at high temperatures does influence the thermal elasticity of phase egg. In addition, all our HPHT experimental  $P$ - $V$  data at 300 K above 14 GPa were annealed from high temperature condition and the hydrogen bond equilibrium was not reached on the experimental time scale, leading to the absence of

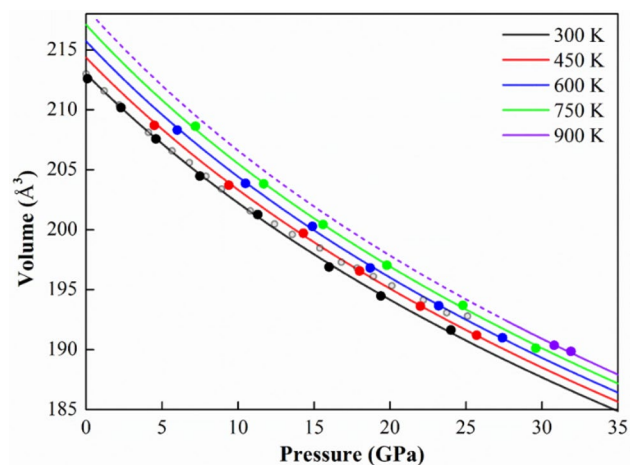


**Fig. 2**  $P$ - $V$ - $T$  data obtained for phase egg in this study. The solid or dashed lines represent the isothermal compression curves from the high-temperature third-order B-M EoS at 300 K, 450 K, 600 K, 750 K and 900 K. The gray circles represent the high-pressure experimental data at room temperature in this study

the new hydrogen bond configuration at 300 K at HPHT experiments.

### Axial compressibility

The trend of lattice parameters relative  $a$  ( $a/a_0$ ),  $b$  ( $b/b_0$ ),  $c$  ( $c/c_0$ ) and  $\beta$  angle with pressure are plotted in Fig. 3. The compressibility of unit-cell axes is significant anisotropic below 14 GPa at room temperature, the shortest axis  $b$  is the softest direction and the longest axis  $a$  is most compressible direction. The kink is also observed in the trend of  $b$ -axis and  $c$ -axis versus pressure at  $\sim 14$  GPa, i.e.,  $b$ -axis and  $c$ -axis become harder to compress. A linearized second-order B-M EoS fitting where each axial dimension is cubed and treated as volume in the B-M formulation was used to compare the axial compressibility. The zero-pressure axial compressibility of linear dimension  $l$ , defined as  $\beta_{l0} = -(l^{-1})(\delta l/\delta P)_{P=0}$ , is related to the linear modulus by  $M_{l0} = (\beta_{l0})^{-1}$ . The fitted linear moduli of  $a$ -axis is 1116(27) GPa among the entire experimental pressure range, and those of  $b$  and  $c$  axes are 312(4) GPa, 585(29) below 14 GPa and 539(37) GPa,

855 (14) GPa above 14 GPa respectively, corresponding to axial compressibility values of  $\beta_a = 0.90(2) \times 10^{-3} \text{ GPa}^{-1}$ ,  $\beta_b = 3.21(4) \times 10^{-3} \text{ GPa}^{-1}$ ,  $\beta_c = 1.71(9) \times 10^{-3} \text{ GPa}^{-1}$  ( $\beta_a$ :  $\beta_b$ :  $\beta_c = 1:3.57:1.90$ ) below 14 GPa and  $\beta_b = 1.86(12) \times 10^{-3} \text{ GPa}^{-1}$ ,  $\beta_c = 1.17(2) \times 10^{-3} \text{ GPa}^{-1}$  ( $\beta_a$ :  $\beta_b$ :  $\beta_c = 1:2.07:1.30$ ) above 14 GPa. The  $\beta$  angle reduces to  $\sim 97.86^\circ$  rapidly from 0 to 9 GPa and it reduces slowly by  $\sim 0.03^\circ$  between 9 and 14 GPa, then remains at a constant value of  $\sim 97.83^\circ$  up to the highest pressure in this study, meaning that the crystal shape is almost no longer distorted above 14 GPa. Present results are in agreement with those of previous single-crystal XRD results except that  $a$ -axis is stiffer than the results from Schulze et al. (2018), but consistent with the powder XRD results (Vanpeteghem et al. 2003). The crystal chemical characteristics at high pressures of phase egg reveal that the distortions of Si and Al octahedra accompanied with volume compression in the studied pressure range (Fig. S3) are consistent with the variation of  $\beta$  angle. The Si–O(4) bond distance is decreased rapidly from 0 to 14 GPa (Fig. S4), which mainly contributes to the compression of  $b$ -axis and  $c$ -axis (Schulze et al. 2018). On the other hand, the axial compressibility of phase egg at high  $P$ – $T$  conditions (Fig. S5) shows that the obvious kink on  $b$ -axis is not observed, indicating that the anisotropy is still significantly under high temperature.

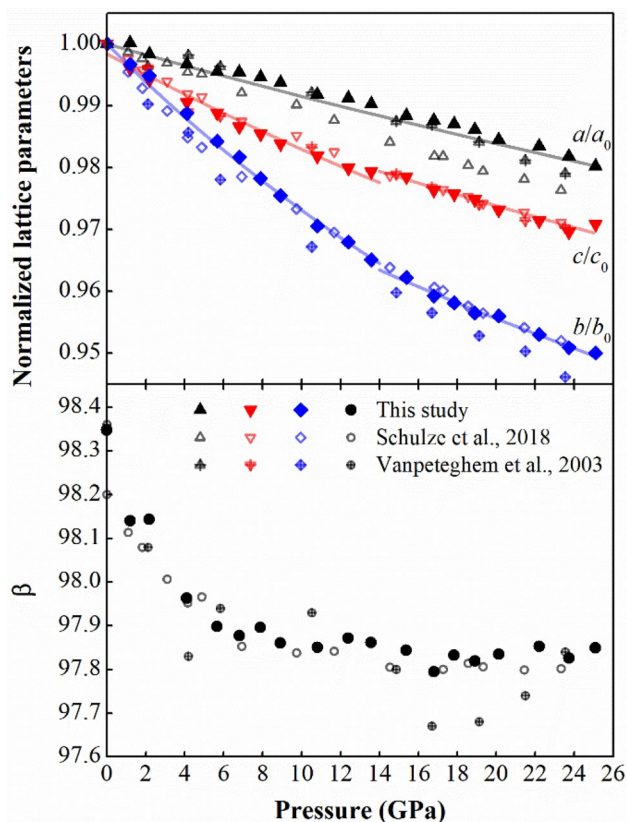


**Fig. 3** a Normalized lattice parameters ( $a/a_0$ ,  $b/b_0$ , and  $c/c_0$ ) and  $\beta$  angle of phase egg as a function of pressure at room temperature. Filled symbols, open symbols and symbols with cross represent the data from this study, Schulze et al. (2018) and Vanpeteghem et al. (2003), respectively

### Behavior of hydrogen atoms

Although it is hard to determine the atomic coordinates of hydrogen atom by single-crystal XRD at high pressure, we managed to conduct the crystal structure refinements which reported in the Table S3 at six different pressures and obtained site parameters of hydrogen atom. The length of O–H covalent bond and hydrogen bond are plotted in Fig. 4a. It is worth noting that the hydrogen site parameters have larger errors due to the small X-ray scattering cross-section of hydrogen, but the trend is reliable. The hydrogen atom moves its position and forms covalent bond with O(3) above 14 GPa in the experimental pressure range, leading to a different hydrogen bond configuration from O(4)–H·O(3) to O(4)·H–O(3) (Fig. 4b), which is consistent with the first-principles calculations (Mookherjee et al. 2019). Our high pressure IR spectra (Fig. 5) provide additional evidence for this structure change. The O–H stretching frequency decreased gradually with increasing of pressure up to  $\sim 8$  GPa, which indicated that the absorption band is controlled by strong hydrogen bond (Libowitzky 1999). However, the absorption band is broadened and the frequency remains relatively constant at about  $3040 \text{ cm}^{-1}$  between 8 and 13 GPa. The length of H·O hydrogen bond gets shorter and O–H covalent bond gets longer with the increase of pressure. And the energies of the low- and high-pressure phase are very close near the transition pressure according to the

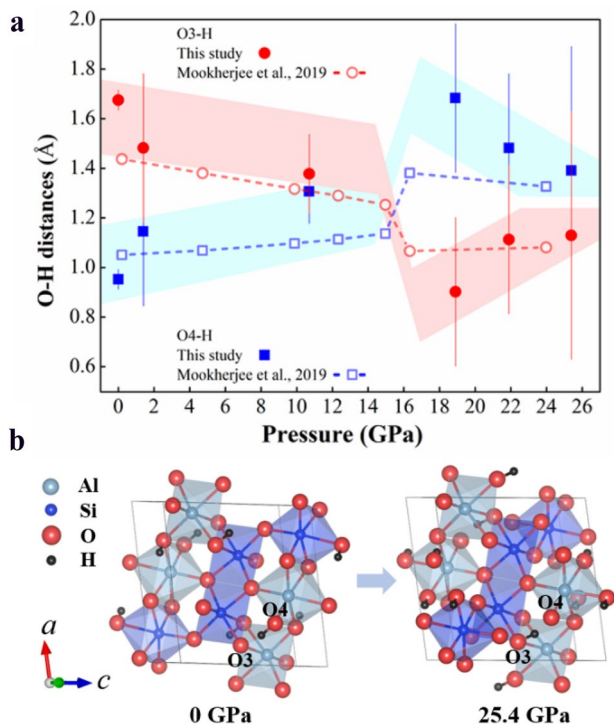


**Fig. 4** **a** The evolution of hydrogen bond in phase egg under pressure at room temperature. The hydrogen atom flips its position at ~14 GPa, and hydrogen bond configuration changes from O(4)–H···O(3) to O(4)···H–O(3). **b** The crystal structure of phase egg at ambient condition and at 25.4 GPa and room temperature. The structure model reported by Schmidt et al. (1998) was used to conduct the structure refinement at ambient condition and the atomic coordinates of previous pressure were used as starting parameters at high pressures. Light-blue and dark-blue octahedra represent AlO<sub>6</sub> and SiO<sub>6</sub>. Hydrogen atoms and oxygen atoms are shown in black and red balls, respectively

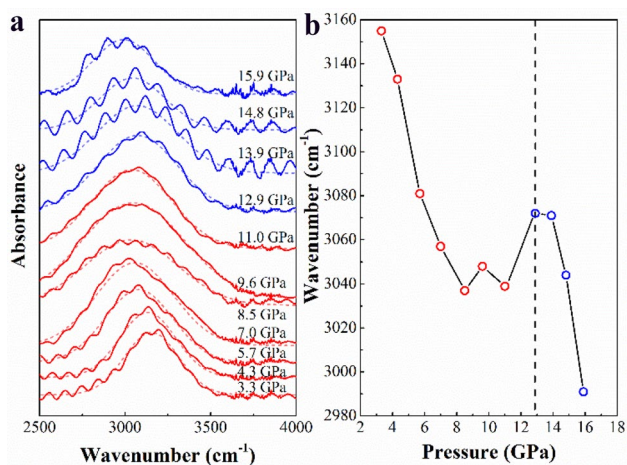


**Fig. 5** **a** In situ typical IR spectra of phase egg at high pressures and room temperature. **b** IR absorption bands of phase egg were plotted as a function of pressure

theoretical calculations (Mookherjee et al. 2019). Thus, the behaviors of IR absorption band between 8 and 13 GPa are most likely caused by the disordered state of hydrogen atom, i.e., partial occupancy of the two sites. A similar disordered state of hydrogen atoms in  $\delta$ -AlOOH has been observed before hydrogen bond symmetrization based on the neutron diffraction experiments at room temperature (Sano-Furukawa et al. 2018). In addition, this variation character corresponds to the variation trend of beta angle, indicating the effects of the state of hydrogen bond on compressibility. The IR absorption band jumped back to the high frequency side, revealing that a new shorter O–H bond formed and the configuration of hydrogen bond changed at ~13 GPa. The small discrepancy on the transition pressure between the XRD and IR results may be caused by the different pressure indicator and transmitting medium.

The hydrogen bond in high-pressure hydrous phases has attracted much attention for years. It generally takes an asymmetric configuration at ambient pressure, exhibiting that the covalent bond O–H is shorter than H···O hydrogen bond and the O–H···O configuration is nonlinear. However, hydrogen bond is significantly affected by pressure and the energy barrier between double-well energy potential for the hydrogen motion will be depressed with increasing pressure (Zha et al. 2016), it is predicted to become symmetric which proton located at the center of two oxygen atoms at high pressure. The hydrogen bond symmetrization has been investigated in ice phases (Goncharov et al. 1996; Lu et al. 2010; Tsuchiya and Tsuchiya 2017) and many hydrous phases including  $\delta$ -AlOOH (Sano-Furukawa et al. 2009, 2018; Tsuchiya and Tsuchiya 2009; Mashino et al. 2016; Kang et al. 2017), phase D (Tsuchiya et al. 2005; Hushur et al. 2011; Wu et al. 2016), phase H (Tsuchiya and Mookherjee 2015; Panero and Caracas 2017) and phase Pi (Peng et al. 2017). However, phase egg exhibits another configuration of hydrogen bond at high pressure based on our single-crystal XRD and IR experiments as well as the theoretical calculations (Mookherjee et al. 2019). The presence of hydrogen bond could affect the distortion degree of the neighbor octahedron (Wu et al. 2016), which can help to explain that the length of Si–O(4) is much longer than the rest of bonds in Si–O octahedron at ambient condition. The orientation of hydrogen bond in the crystal structure of phase egg is mainly aligned along *b*-axis and has a component along *c*-axis (Mookherjee et al. 2019), leading to the obvious anisotropy of the axial compressibility below 14 GPa. On the other hand, the properties of hydrogen bond affect the geometry of the neighbor Si–O bond under compression, the length of Si–O(3) increased slightly below 14 GPa could be a response to the change of hydrogen bond configuration. The compression mechanism of phase egg is mainly driven by the shortening of Si–O(4) bond below 14 GPa, but the new hydrogen bond configuration affects

the compression mechanism and makes it difficult to compress above 14 GPa (Vanpeteghem et al. 2003; Mookherjee et al. 2019). Therefore, the abnormal changes of volume and the bond lengths of Si–O(4) and Si–O(3) below and above 14 GPa in this study should be attributed to the change of hydrogen bond configuration in phase egg.

Hydrogen bond itself and its change induced by pressure have significant effects on the properties of host phases. The symmetric hydrogen bonds have predicted to increase the bulk modulus  $K_0$  for  $\delta$ -AlOOH by ~44% (Sano-Furukawa et al. 2009), phase H by 31% (Tsuchiya and Mookherjee 2015) and phase D by 18% (Hushur et al. 2011) (Table S4). Similarly, the change of hydrogen bond configuration for phase egg also leads to an increase of  $K_0$  by ~35% at room temperature. Such a significant change in bulk modulus will lead to important effects on geophysical observation. Nevertheless, hydrogen bond equilibrium is controlled by a combination of thermodynamics and quantum mechanics (Dougherty 1998). The high-pressure experiments under room temperature cannot reflect the properties of minerals under the mantle conditions. Our HPHT experiments results show that there is no discontinuity on compressibility, implying the temperature effects on the state of hydrogen atom. The thermally induced disordering of hydrogen atom smears over its configuration under HPHT conditions and it significantly affects the thermal elasticity of phase egg. The consideration on temperature provides more uncertainties in the research on physical properties of minerals. Therefore, it is necessary to further study the state of hydrogen at the HPHT conditions on other hydrous phases.

## Implications for the subduction zone

Although the content of water in Earth's interior is still under debate, it has been estimated that about one third of water trapped by the slabs could be transported into the deep mantle (van Keken et al. 2011). Aluminous hydrous phases have significant greater thermal stability than the magnesio-silicate hydrous phases and are likely to be stable along the normal mantle geotherm (Nishi et al. 2019). Recent experiments show that Al-phase D is stable at temperatures over 2000 °C at 26 GPa, at least 800 °C higher than the Mg-phase D endmember (Pamato et al. 2014). The sediments and oceanic crusts contain greater amounts of alumina and silica than the mafic mantle rocks, and the phases in ASH ternary system are most likely to be the potential water carriers in subduction zones. HPHT experiments have been conducted to confirm the stability fields of topaz-OH, phase egg and  $\delta$ -AlOOH accordingly, a series of reactions among these phases provide a continuous chain which can transport water from the upper mantle to the core-mantle boundary (Ono

1998; Sano et al. 2004; Fukuyama et al. 2017; Duan et al. 2018).

We have evaluated the density and bulk velocity profiles of phase egg as a function of pressure along 300 K, 1000 K, 1300 K, 1500 K and 1700 K isotherms (Fig. 6) using the thermoelastic parameters at the mantle transition zone conditions to understand the significance of our results in geophysics. Our modeled results show that the density of phase egg is denser than the preliminary reference Earth model (PREM) (Dziewonski and Anderson 1981) at the mantle transition zone along both the cold and warm subducting slab geotherms, indicating that the presence of phase egg will contribute a positive force for subduction despite that

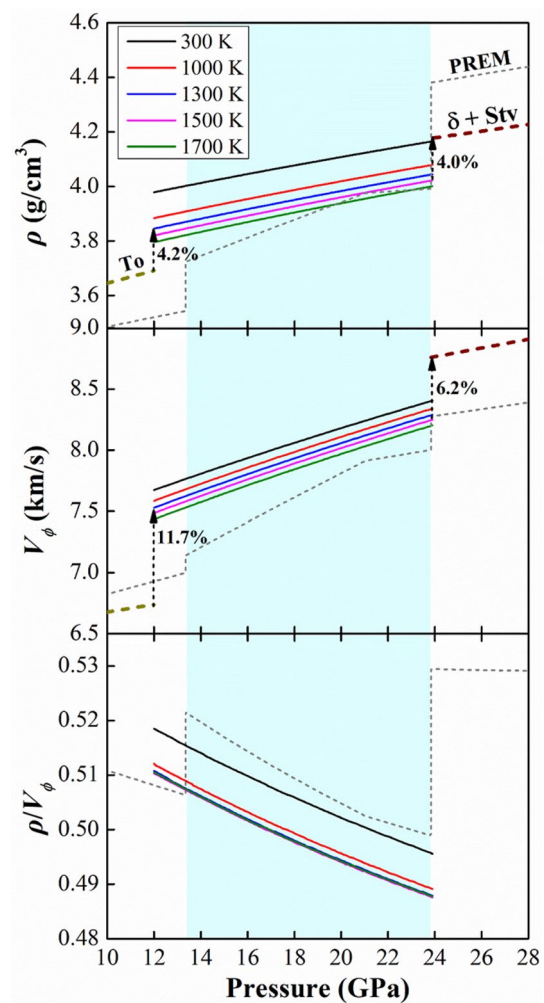


**Fig. 6** Density ( $\rho$ ), bulk sound velocity ( $V_\phi$ ) and  $\rho/V_\phi$  of phase egg which have been compared with topaz-OH (To) at 1300 K (Gatta et al. 2014),  $\delta$ -AlOOH ( $\delta$ ) + stishovite (Stv) at 1500 K (Duan et al. 2018) and the preliminary reference Earth model (PREM) (Dziewonski and Anderson 1981). Here, we assumed that the geotherms of cold, warm and hot subducting slabs and normal mantle geotherm are 1000 K, 1300 K, 1500 K and 1700 K at the depth of mantle transition zone

its proportion may be very limited. The velocity profiles of phase egg along the cold and warm subducting slab geotherms and even the normal mantle geotherm are faster than the PREM, but it has a lower  $\rho/V_{\phi}$  ratio (Dziewonski and Anderson 1981). These results are useful to identify the potential presence of phase egg and may provide a constraint on the velocity anomaly in subduction zones. It is assumed that topaz-OH can react with stishovite and form phase egg at 12 GPa and 1300 K (Ono 1998), while phase egg decomposes into  $\delta$ -AlOOH and stishovite at 23.5 GPa and 1500 K (Fukuyama et al. 2017; Duan et al. 2018). We modeled the changes of density and bulk sound velocity across these phases transition. Here, we assumed that the thermal elastic parameters of topaz-OH same as phase egg for the reason that there are no available parameters, we calculated its  $\rho$  and  $V_{\phi}$  profiles combined with the elastic parameters from Gatta et al. (2014). Our modeled results show that the density and bulk sound velocity of phase egg are much higher than topaz-OH, the phase transition from topaz-OH to phase egg induces an abrupt increase in  $\rho$  ( $\sim 4.2\%$ ) and  $V_{\phi}$  ( $\sim 11.7\%$ ) along the warm subducting slab geotherm at the base of upper mantle. As to the scene that phase egg decomposes into  $\delta$ -AlOOH and stishovite at the base of mantle transition zone or the top of lower mantle, it will lead to the density and bulk velocity increased by  $\sim 4.0\%$  and  $\sim 6.2\%$  respectively along the hot subducting slab geotherm (Duan et al. 2018), providing a positive contribution to the 660 km discontinuity. At Earth's mantle conditions, the effect of lattice preferred orientation (LPO) on seismic velocity of hydrous minerals which may exist in subducted slabs should be considered (Wu et al. 2017). Furthermore, iron is the most abundant transition metal in Earth's mantle and may significantly affect the physical properties of mantle mineral phases. The spin transition of Fe-bearing minerals in Earth's mantle has been reported to have significant effects on density, compressibility, elasticity, and sound velocity of the host minerals (Wu et al. 2016), and the evolution of hydrogen bond might have relationship with the spin crossover of  $\text{Fe}^{3+}$  (Thompson et al. 2017). Therefore, the further consideration on the effects of LPO and Fe-doped in phase egg will give more implications on the aluminosilicate hydrous phases.

## Summary

In summary, we have observed that hydrogen atom flips its position of phase egg at  $\sim 14$  GPa and room temperature, confirming the opinion of previous theoretical prediction at 0 K. However, this behavior is smeared out because of thermal disordering of hydrogen atom at high temperatures. We propose that the properties of hydrogen bond itself and its effects on the hydrous phases reported at high pressure

and room temperature should be reappraised with the high temperature effects. The obtained thermoelastic parameters of phase egg were applied to model the density and bulk velocity profiles along the subducting slab geotherm, which is useful to decipher the seismic signature. We further simulated the increase in density ( $\sim 4.0\%$  and  $\sim 4.2\%$ ) and bulk velocity ( $\sim 6.2\%$  and  $\sim 11.7\%$ ) among the phase transition from topaz-OH to phase egg and then to  $\delta$ -AlOOH and stishovite. The present results provide new constraints on the existing state of hydrogen in Earth's interior, deep-water transportation and geophysical observation.

**Acknowledgements** X. Wu acknowledge financial support from the National Science Foundation of China (41827802). We would like to thank Sergey Tkachev for gas loading the diamond anvil cells, Jingui Xu for help in XRD data analysis, Haipeng Song and Xiang Li for help in infrared spectra experiments. This work was performed at GeoSoilEnviroCARS and HPCAT, Advanced Photon Source (APS), Argonne National Laboratory (ANL). HPCAT operations are supported by DOE-NNSA under Award No. DE-NA0001974 and DOE-BES under Award No. DE-FG02-99ER45775. GeoSoilEnviroCARS operations are supported by the National Science Foundation-Earth Sciences (EAR-1128799) and the Department of Energy, Geosciences (DE-FG02-94ER14466). APS is supported by DOE-BES, under Contract No. DE-AC02-06CH11357. The high-pressure IR experiments were performed at National Synchrotron Radiation Laboratory (NSRL), China.

**Author contributions** Conceptualization: XW; methodology: YL, RH, YW; formal analysis and investigation: YL; writing original draft preparation: YL; writing review and editing: XW, YL, JZ; funding acquisition: XW; resources: DZ; supervision: XW.

**Funding** This study was funded by National Science Foundation of China (Grant number 41827802).

## Compliance with ethical standards

**Conflict of interest** The authors declare that they have no conflict of interest.

## References

- Angel RJ, Alvaro M, Gonzalez-Platas J (2014) EosFit7c and a Fortran module (library) for equation of state calculations. *Zeitschrift für Kristallographie Cryst Mater* 229:405–419. <https://doi.org/10.1515/zkri-2013-1711>
- Dera P, Zhuravlev K, Prakapenka V, Rivers ML, Finkelstein GJ, Grubor-Urosevic O et al (2013) High pressure single-crystal micro X-ray diffraction analysis with GSE\_ADA/RSV software. *High Press Res* 33:466–484. <https://doi.org/10.1080/08957959.2013.806504>
- Dolomanov OV, Bourhis LJ, Gildea RJ, Howard JAK, Puschmann H (2009) OLEX2: a complete structure solution, refinement and analysis program. *J Appl Crystallogr* 42:339–341. <https://doi.org/10.1107/s0021889808042726>
- Dougherty RC (1998) Temperature and pressure dependence of hydrogen bond strength: a perturbation molecular orbital approach. *J Chem Phys* 109:7372–7378. <https://doi.org/10.1063/1.477343>

- Duan Y, Sun N, Wang S, Li X, Guo X, Ni H et al (2018) Phase stability and thermal equation of state of  $\delta$ -AlOOH: implication for water transportation to the deep lower mantle. *Earth Planet Sci Lett* 494:92–98. <https://doi.org/10.1016/j.epsl.2018.05.003>
- Dziewonski AM, Anderson DL (1981) Preliminary reference Earth model. *Phys Earth Planet Inter* 25:297–356. [https://doi.org/10.1016/0031-9201\(81\)90046-7](https://doi.org/10.1016/0031-9201(81)90046-7)
- Eggleton RA, Boland JN, Ringwood AE (1978) High pressure synthesis of a new aluminum silicate  $\text{Al}_3\text{Si}_5\text{O}_{17}(\text{OH})$ . *Geochem J* 12:191–194
- Faccenda M (2014) Water in the slab: a trilogy. *Tectonophysics* 614:1–30. <https://doi.org/10.1016/j.tecto.2013.12.020>
- Fei Y, Ricolleau A, Frank M, Mibe K, Shen G, Prakapenka V (2007) Toward an internally consistent pressure scale. *Proc Natl Acad Sci USA* 104:9182–9186. <https://doi.org/10.1073/pnas.0609013104>
- Fukuyama K, Ohtani E, Shibazaki Y, Kagi H, Suzuki A (2017) Stability field of phase Egg,  $\text{AlSiO}_3\text{OH}$  at high pressure and high temperature: possible water reservoir in mantle transition zone. *J Mineral Petrol Sci* 112:31–35. <https://doi.org/10.2465/jmps.160719e>
- Gatta GD, Morgenroth W, Dera P, Petitgirard S, Liermann HP (2014) Elastic behavior and pressure-induced structure evolution of topaz up to 45 GPa. *Phys Chem Miner* 41:569–577. <https://doi.org/10.1007/s00269-014-0670-4>
- Goncharov AF, Struzhkin VV, Somayazulu MS, Hemley RJ, Mao HK (1996) Compression of ice to 210 Gigapascals: infrared evidence for a symmetric hydrogen-bonded phase. *Science* 273:218–220. <https://doi.org/10.1126/science.273.5272.218>
- Hammersley AP (2016) FIT2D: a multi-purpose data reduction, analysis and visualization program. *J Appl Crystallogr* 49:646–652. <https://doi.org/10.1107/s1600576716000455>
- Holland TJB, Redfern SAT (1997) Unit cell refinement from powder diffraction data: the use of regression diagnostics. *Mineral Mag* 61:65–77. <https://doi.org/10.1180/minmag.1997.061.404.07>
- Howe H, Pawley AR (2019) The effect of solid solution on the stability of talc and 10-Å phase. *Contrib Miner Pet* 174:81. <https://doi.org/10.1007/s00410-019-1616-0>
- Hushur A, Manghnani MH, Smyth JR, Williams Q, Hellebrand E, Lonappan D et al (2011) Hydrogen bond symmetrization and equation of state of phase D. *J Geophys Res*. <https://doi.org/10.1029/2010jg008087>
- Kang D, Feng YX, Yuan Y, Ye QJ, Zhu F, Huo HY et al (2017) Hydrogen-bond symmetrization of  $\delta$ -AlOOH. *Chin Phys Lett* 34:108301. <https://doi.org/10.1088/0256-307x/34/10/108301>
- Libowitzky E (1999) Correlation of O–H stretching frequencies and O–H···O hydrogen bond lengths in minerals. *Monatsh Chem* 130:1047–1059. <https://doi.org/10.1007/BF03354882>
- Litasov KD, Ohtani E (2007) Effect of water on the phase relations in Earth's mantle and deep water cycle. *Geol Soc Am Spec Pap* 421:115–156. [https://doi.org/10.1130/2007.2421\(08\)](https://doi.org/10.1130/2007.2421(08))
- Liu Z, Park J, Karato S (2018) Seismic evidence for water transport out of the mantle transition zone beneath the European Alps. *Earth Planet Sci Lett* 482:93–104. <https://doi.org/10.1016/j.epsl.2017.10.054>
- Lu XZ, Zhang Y, Zhao P, Fang SJ (2010) Vibrational analysis of the hydrogen-bond symmetrization in ice. *J Phys Chem B* 115:71–74. <https://doi.org/10.1021/jp1074434>
- Mao HK, Xu J, Bell PM (1986) Calibration of the ruby pressure gauge to 800 kbar under quasi-hydrostatic conditions. *J Geophys Res*. <https://doi.org/10.1029/JB091iB05p04673>
- Mashino I, Murakami M, Ohtani E (2016) Sound velocities of delta-AlOOH up to core-mantle boundary pressures with implications for the seismic anomalies in the deep mantle. *J Geophys Res Solid Earth* 121:595–609. <https://doi.org/10.1002/2015JB012477>
- Momma K, Izumi F (2008) VESTA: a three-dimensional visualization system for electronic and structural analysis. *J Appl Crystallogr* 41:653–658. <https://doi.org/10.1107/s0021889808012016>
- Mookherjee M, Panero WR, Wunder B, Jahn S (2019) Anomalous elastic behavior of phase egg,  $\text{AlSiO}_3(\text{OH})$ , at high pressures. *Am Miner* 104:130–139. <https://doi.org/10.2138/am-2019-6694>
- Muir JMR, Brodholt JP (2018) Water distribution in the lower mantle: implications for hydrolytic weakening. *Earth Planet Sci Lett* 484:363–369. <https://doi.org/10.1016/j.epsl.2017.11.051>
- Nishi M, Irifune T, Tsuchiya J, Tange Y, Nishihara Y, Fujino K, Higo Y (2014) Stability of hydrous silicate at high pressures and water transport to the deep lower mantle. *Nat Geosci* 7:224–227. <https://doi.org/10.1038/ngeo2074>
- Nishi M, Tsuchiya J, Kuwayama Y, Arimoto T, Tange Y, Higo Y et al (2019) Solid solution and compression behavior of hydroxides in the lower mantle. *J Geophys Res Solid Earth* 124:10231–10239. <https://doi.org/10.1029/2019jb018146>
- Ohtani E (2005) Water in the mantle. *Elements* 1:25–30. <https://doi.org/10.2113/gselements.1.1.25>
- Ohtani E, Litasov K, Suzuki A, Kondo T (2001) Stability field of new hydrous phase,  $\delta$ -AlOOH, with implications for water transport into the deep mantle. *Geophys Res Lett* 28:3991–3993. <https://doi.org/10.1029/2001gl013397>
- Ohtani E, Litasov K, Hosoya T, Kubo T, Kondo T (2004) Water transport into the deep mantle and formation of a hydrous transition zone. *Phys Earth Planet Inter* 143–144:255–269. <https://doi.org/10.1016/j.pepi.2003.09.015>
- Ono S (1998) Stability limits of hydrous minerals in sediment and mid-ocean ridge basalt compositions: implications for water transport in subduction zones. *J Geophys Res Solid Earth* 103:18253–18267. <https://doi.org/10.1029/98jb01351>
- Pamato MG, Myhill R, Ballaran TB, Frost DJ, Heidelbach F, Miyajima N (2014) Lower-mantle water reservoir implied by the extreme stability of a hydrous aluminosilicate. *Nat Geosci* 8:75–79. <https://doi.org/10.1038/ngeo2306>
- Panero WR, Caracas R (2017) Stability of phase H in the  $\text{MgSiO}_4\text{H}_2$ – $\text{AlOOH}$ – $\text{SiO}_2$  system. *Earth Planet Sci Lett* 463:171–177. <https://doi.org/10.1016/j.epsl.2017.01.033>
- Pearson DG, Brenker FE, Nestola F, McNeill J, Nasdala L, Hutchison MT et al (2014) Hydrous mantle transition zone indicated by ringwoodite included within diamond. *Nature* 507:221–224. <https://doi.org/10.1038/nature13080>
- Peng Y, Mookherjee M, Hermann A, Bajgajn S, Liu S, Wunder B (2017) Elasticity of phase-Pi ( $\text{Al}_3\text{Si}_2\text{O}_7(\text{OH})_3$ )—a hydrous aluminosilicate phase. *Phys Earth Planet Inter* 269:91–97. <https://doi.org/10.1016/j.pepi.2017.05.016>
- Rivers M, Prakapenka V, Kubo A, Pullins C, Holl C, Jacobsen S (2008) The COMPRES/GSECARS gas-loading system for diamond anvil cells at the advanced photon source. *High Press Res* 28:273–292. <https://doi.org/10.1080/08957950802333593>
- Sano A, Ohtani E, Kubo T, Funakoshi K (2004) In situ X-ray observation of decomposition of hydrous aluminum silicate  $\text{AlSiO}_3\text{OH}$  and aluminum oxide hydroxide  $\delta$ -AlOOH at high pressure and temperature. *J Phys Chem Solids* 65:1547–1554. <https://doi.org/10.1016/j.jpcs.2003.12.015>
- Sano-Furukawa A, Kagi H, Nagai T, Nakano S, Fukura S, Ushijima D et al (2009) Change in compressibility of  $\delta$ -AlOOH and  $\delta$ -AlOOD at high pressure: a study of isotope effect and hydrogen-bond symmetrization. *Am Miner* 94:1255–1261. <https://doi.org/10.2138/am.2009.3109>
- Sano-Furukawa A, Hattori T, Komatsu K, Kagi H, Nagai T, Molaison JJ et al (2018) Direct observation of symmetrization of hydrogen bond in delta-AlOOH under mantle conditions using neutron diffraction. *Sci Rep* 8:15520. <https://doi.org/10.1038/s41598-018-33598-2>
- Schmidt MW (1995) Lawsonite: upper pressure stability and formation of higher density hydrous phases. *Am Miner* 80:1286–1292. <https://doi.org/10.2138/am-1995-11-1219>

- Schmidt MW, Finger LW, Angel RJ, Dinnebier RE (1998) Synthesis, crystal structure, and phase relations of  $\text{AlSiO}_3\text{OH}$ , a high-pressure hydrous phase. *Am Miner* 83:881–888. <https://doi.org/10.2138/am-1998-7-820>
- Schulze K, Pamato MG, Kurnosov A, Ballaran TB, Glazyrin K, Pakhomova A, Marquardt H (2018) High-pressure single-crystal structural analysis of  $\text{AlSiO}_3\text{OH}$  phase egg. *Am Miner* 103:1975–1980. <https://doi.org/10.2138/am-2018-6562>
- Thompson EC, Campbell AJ, Tsuchiya J (2017) Elasticity of  $\epsilon\text{-FeOOH}$ : seismic implications for Earth's lower mantle. *J Geophys Res Solid Earth* 122:5038–5047. <https://doi.org/10.1002/2017jb014168>
- Tschauner O, Huang S, Greenberg E, Prakapenka VB, Ma C, Rossman GR et al (2018) Ice-VII inclusions in diamonds evidence for aqueous fluid in Earth's deep mantle. *Science* 359:1136–1139. <https://doi.org/10.1126/science.aao3030>
- Tsuchiya J, Mookherjee M (2015) Crystal structure, equation of state, and elasticity of phase H ( $\text{MgSiO}_4\text{H}_2$ ) at Earth's lower mantle pressures. *Sci Rep*. <https://doi.org/10.1038/srep15534>
- Tsuchiya J, Tsuchiya T (2009) Elastic properties of  $\delta\text{-AlOOH}$  under pressure: first principles investigation. *Phys Earth Planet Inter* 174:122–127. <https://doi.org/10.1016/j.pepi.2009.01.008>
- Tsuchiya J, Tsuchiya T (2017) First principles calculation of the elasticity of ice VIII and X. *J Chem Phys*. <https://doi.org/10.1063/1.4973339>
- Tsuchiya J, Tsuchiya T, Tsuneyuki S (2005) First-principles study of hydrogen bond symmetrization of phase D under high pressure. *Am Miner* 90:44–49. <https://doi.org/10.2138/am.2005.1628>
- van Keken PE, Hacker BR, Syracuse EM, Abers GA (2011) Subduction factory: 4. Depth-dependent flux of  $\text{H}_2\text{O}$  from subducting slabs worldwide. *J Geophys Res*. <https://doi.org/10.1029/2010jb007922>
- Vanpeteghem CB, Ohtani E, Kondo T, Takemura K, Kikegawa T (2003) Compressibility of phase egg  $\text{AlSiO}_3\text{OH}$  equation of state and role of water at high pressure. *Am Miner* 88:1408–1411. <https://doi.org/10.2138/am-2003-1002>
- Wirth R, Vollmer C, Brenker F, Matsyuk S, Kaminsky F (2007) Inclusions of nanocrystalline hydrous aluminium silicate “Phase Egg” in superdeep diamonds from Juina (Mato Grosso State, Brazil). *Earth Planet Sci Lett* 259:384–399. <https://doi.org/10.1016/j.epsl.2007.04.041>
- Wu X, Wu Y, Lin JF, Liu J, Mao Z, Guo X et al (2016) Two-stage spin transition of iron in FeAl-bearing phase D at lower mantle. *J Geophys Res Solid Earth* 121:6411–6420. <https://doi.org/10.1002/2016jb013209>
- Wu X, Lin JF, Kaercher P, Mao Z, Liu J, Wenk HR, Prakapenka VB (2017) Seismic anisotropy of the D' layer induced by (001) deformation of post-perovskite. *Nat Commun* 8:14669. <https://doi.org/10.1038/ncomms14669>
- Xue X (2006) Cation order and hydrogen bonding of high-pressure phases in the  $\text{Al}_2\text{O}_3\text{-SiO}_2\text{-H}_2\text{O}$  system: an NMR and Raman study. *Am Miner* 91:850–861. <https://doi.org/10.2138/am.2006.2064>
- Yoshino T, Baker E, Duffey K (2019) Fate of water in subducted hydrous sediments deduced from stability fields of FeOOH and AlOOH up to 20 GPa. *Phys Earth Planet Inter*. <https://doi.org/10.1016/j.pepi.2019.106295>
- Zha CS, Tse JS, Bassett WA (2016) New Raman measurements for  $\text{H}_2\text{O}$  ice VII in the range of  $300\text{ cm}^{-1}$  to  $4000\text{ cm}^{-1}$  at pressures up to 120 GPa. *J Chem Phys*. <https://doi.org/10.1063/1.4963320>

**Publisher's Note** Springer Nature remains neutral with regard to jurisdictional claims in published maps and institutional affiliations.